Journal of Computational Physics **171,** 776–804 (2001)
doi:10.1006/jcph.2001.6810, available online at http://www.idealibrary.com on IDEAL®

Coupling of the Interface Tracking and the Two-Fluid Models for the Simulation of Incompressible Two-Phase Flow

Gregor Černe,*,[1] Stojan Petelin,† and Iztok Tiselj*

*Reactor Engineering Division, Jožef Stefan Institute and †Faculty of Maritime Studies and Transport, University of Ljubljana, Jamova 39, 1000 Ljubljana, Slovenia

Received May 23, 2000; revised April 12, 2001

The volume of fluid (VOF) method, which uses an interface tracking algorithm for the simulation of the two-phase flow, is coupled with the "two-fluid" model, which is based on time and space averaged equations and cannot track the interface explicitly. The idea of the present work is to use the VOF method in the parts of the computational domain where the grid density allows surface tracking. In the parts of the domain where the flow is too dispersed to be described by the interface tracking algorithms, the two-fluid model is used. The equations of the two-fluid model are less accurate than the VOF model due to the empirical closures required in the averaged equations. However, in the case of the sufficiently dispersed flow, the two-fluid model results are still much closer to the real world than the results of the VOF method, which do not have any physical meaning when the grid becomes too coarse. Each model in the present work uses a separate set of equations suitable for description of two-dimensional, incompressible, viscous two-phase flow. Similar discretization techniques are used for both sets of equations and solved with the same numerical method. Coupling of both models is achieved via the volume fraction of one of the fluids, which is used in both models. A special criterion for the transition between the models is derived from the interface reconstruction function in the VOF method. An idealized vortical flow and the Rayleigh–Taylor instability are used as tests of the coupling. In both cases the time development causes mixing of the fluids and dispersion of the interface that is beyond the capabilities of the model based on the VOF method. Therefore the two-fluid model gradually replaces the interface tracking model. In the final stages of the Rayleigh–Taylor instability, when both fluids are approaching their final positions and the tractable interface appears again, the two-fluid model is gradually replaced by the VOF method.

Key Words: two-phase flow; two-fluid model; interface tracking; volume of fluid model; Rayleigh–Taylor instability; fluid dispersion; stratification.

[1] To whom correspondence should be addressed. Fax: (386) 1 5612 335. E-mail: gregor.cerne@ijs.si.

0021-9991/01 $35.00

1. INTRODUCTION

Two-phase flow plays an important role in many natural and industrial processes such as combustion, petroleum refining, chemical engineering, nuclear technology, and others [27, 47]. It is a very complex phenomenon, which appears in various forms with different characteristics. The numerical simulation is an important tool for the investigation of the two-phase flow and it makes a significant contribution to the understanding of the two-phase flow characteristics and vice versa—the variance and complexity of two-phase flow stimulate the development of many different mathematical models and numerical tools for its simulation. The mathematical models and the computational methods for the particular types of two-phase flows are usually adapted to the physical characteristic of the phenomena and therefore differ significantly.

The interface tracking methods, which are used for the simulations of the transients with moving discontinuous interfaces [24] are the basic two-phase flow models from the standpoint of the Navier–Stokes equations. Since they are based on the fundamental Navier–Stokes equations they explicitly track the interface. During the calculation they keep the interface sharp and enable the accurate location of the particular fluid at any time during the transient. Such an approach allows direct simulations of the two-phase flow phenomena like the phase change and surface tension [2, 29].

There are many types of interface tracking methods, which can be classified according to their approach used to track the interface. The volume of fluid (VOF) [23] method and level set method [36, 40], which use the static grid to locate the fluids, are very popular for the simulation the two-fluid flow problems with significant changes of the interface topology. They experienced several modifications ([19, 34, 36, 38]), and were applied to a variety two-fluid flow problems. There are also several algorithms, which use Lagrangian approaches to track the interface. The marker-and-cell method (MAC) [21] was one of the first interface tracking methods. Besides the static Eulerian grid it uses massless particles scattered over the fluids, which are transported in a Lagrangian manner to locate a particular fluid. The front tracking methods [17, 45] offer the most explicit way for the interface description. In these methods the massless points are located only on the interface and are linked together in the mesh, which moves together with the fluids. In the fully Lagrangian algorithms [22] the mesh moves together with the fluids and no special tool for interface tracking is needed. Due to the complex mesh handling [1] they are suitable to simulate simple two-fluid flow problems without significant topological changes of the interface.

The novelties and improvements of the interface tracking algorithms are usually demonstrated on a small number of typical two-phase flow transients, such as the Rayleigh–Taylor instability [14, 18, 35], shape and stability of a rising bubble [3, 8, 43], or a falling drop [20]. The improvements of these methods and computer hardware development have enabled some complex simulations, such as the three-dimensional simulation of several rising bubbles [5], merging and fragmentation of drops [31], and precise calculation of the pinching pendant drop [19]. However, the limitation of the interface tracking simulations is obvious: none of the simulations mentioned above crossed the point where the discrete grid could not follow the dispersion of the interface. In a dispersed flow, where chunks of the particular fluid are smaller than the grid cells, the surface tracking is not possible and the results of the interface tracking methods lose their physical meaning. A phenomenon, when an interface tracking algorithm numerically disperses, and/or merges the fluid chunks, and drives the transient, is called “numerical surface tension.” This was first noticed by Glimm

et al. during the simulation of the chaotic stage of the Rayleigh–Taylor instability with the front tracking method [18] and was examined in the vortical flow test with the VOF method by Rider and Kothe [38]. Denser nodalization is usually suggested as a solution to this problem [13].

Since most two-phase flows of practical importance are too dispersed to be resolved with the interface tracking algorithms, it is clear that different approaches are necessary. Modeling of the applicable multi-phase flow was thus based mainly on the averaged Navier–Stokes equations in the past three decades. Despite the weakness common to all averaging schemes—a lack of knowledge of the closure relations—two-phase flow modeling will not be possible without the averaged models in the foreseen future.

The so-called two-fluid models, based on time averaging and described in the textbook of Ishii [26], were among the first averaged models of two-phase flow. Later spatial and statistical averaging were used by different authors [15, 42], resulting in similar two-fluid model equations. A typical two-fluid model for a general two-phase flow, used, for example, in nuclear thermal-hydraulics [6], is one-dimensional and consists of the continuity, momentum, and energy balance equation for each phase. Results of the simulations are often unreliable, due to the large uncertainty of the interfacial mass, momentum, and energy exchange terms. These uncertainties are caused by different flow regimes, which can appear in the two-phase flows.

More accurate two-fluid models are available for a dispersed flow [9], especially when the dispersed phase represents solid particles and the interfacial area is exactly known. Bubbly or droplet two-phase flow are more complicated than the solid particle flows, since the interfacial surface is changing. However, two-fluid models for such flows are still much more accurate than the general two-fluid models [6] that attempt to describe all two-phase flow regimes.

This work presents the coupling of both models, which retains the accuracy of the interface tracking schemes for a simple two-phase flow and eliminates the need for the special closure relations of the two-fluid models for the same simple flow. When the flow is dispersed and the interface tracking becomes impossible, a relatively accurate two-fluid model is available. Among many different well-established interface tracking algorithms the VOF method is assumed to be the most convenient, because the color function in the VOF model and volume fraction in the two-fluid model actually represent the same variable. This variable represents the basis of the proposed coupling mechanism.

Two tests are used to analyze the coupling. The first is the idealized problem of the vortex flow by Rider and Kothe [38], where the coupling algorithm is tested by advection and vorticity. The second is a physical problem of the Rayleigh–Taylor instability in a closed tank. This problem was examined numerically and experimentally many times in the past and it serves as a benchmark test for the interface tracking algorithms. In the present work the whole phenomenon is simulated until the fluids completely exchange their positions and the system becomes stable. Jacqmin [28] simulated a similar case with a phase-field model; however, in his particular case of Rayleigh–Taylor instability the characteristic length scale of the dispersed chunks was larger than the grid size so the method did not fail. In our case, the dispersion is far beyond the capabilities of the interface tracking method and both methods are required to simulate the transient.

In the next two sections the main characteristics of the applied VOF model and the two-fluid model are pointed out. The fourth section is dedicated to the description of the coupling, and the fifth section describes the switch mechanism between the VOF and

the two-fluid model. The sixth section reports the results of the idealized vortex flow and the Rayleigh–Taylor instability simulated with the coupled model and the last section gives the conclusions.

2. A MODEL BASED ON THE VOF METHOD

A model based on the VOF method is suitable for describing two-phase problems, where the characteristic length of the interface shape is larger than the grid size. This model describes the two-phase flow by the Navier–Stokes system consisting of a continuity and momentum balance equation. For the two-dimensional system of incompressible viscous fluids these continuity and momentum equations are usually used [37, 43]

$$\nabla \cdot \vec{u} = 0, \tag{1}$$

$$\rho \frac{\partial \vec{u}}{\partial t} + \rho(\vec{u} \cdot \nabla)\vec{u} = \rho\vec{g} - \nabla p + \nabla \cdot (\mu D), \tag{2}$$

where $\vec{u} = (u(x, y, t), v(x, y, t))$ is a two-dimensional velocity field, $p = p(x, y, t)$ is a pressure field, $D = (\nabla\vec{u} + \nabla\vec{u}^T)/2$ is a viscous stress tensor, and $\vec{g}$ is a gravity. Both fluids are treated with the same equations, where the density $\rho(x, y, t)$ and the viscosity $\mu(x, y, t)$ are functions of space and time denoting either the first or the second fluid. The surface tension force does not play an important role in the process of model coupling; therefore it is omitted in the present work. If there is a need for the surface tension modeling it can be included without any essential change to the model coupling.

2.1. *The Interface Tracking Algorithm*

The interface tracking in the VOF method is based on the color function, which marks the fluids in the following way [37]

$$f(x, y) = \begin{cases} 1 & \textit{if place } (x, y) \textit{ is occupied by the fluid } 1 \\ 0 & \textit{if place } (x, y) \textit{ is occupied by the fluid } 2. \end{cases} \tag{3}$$

The function f is evaluated on the discrete grid as a volume average

$$f_{i,j} = \frac{1}{V_{i,j}} \int_{V_{i,j}} f(x, y)\, dV, \tag{4}$$

where $V_{i,j}$ is the volume of the cell (i, j). The interface tracking algorithm consists of the interface reconstruction and an advection algorithm.

The interface reconstruction algorithm is not unique. There are several algorithms with different accuracy and complexity. The LVIRA algorithm [37] is used for the reconstruction of the interface in our work. This algorithm makes a linear approximation of the interface by putting a line segment in each multi-fluid cell, i.e., in each cell which has $0 < f_{i,j} < 1$. The approximate interface orientation in the cell (i, j) is determined from the volume fractions in a 3×3 block of neighboring cells. The orientation of each interface segment is determined

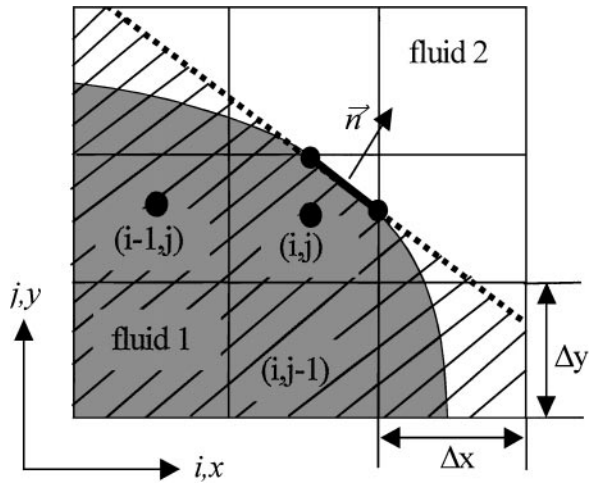

FIG. 1. Interface reconstruction with the LVIRA algorithm.

by the normal vector $\vec{n}$, which is calculated by the minimization of the function

$$G_{i,j}(\vec{n}) = \sum_{l=-1}^{1} \sum_{k=-1}^{1} (f_{i+k,j+l} - f'_{i+k,j+l}(\vec{n}))^2. \tag{5}$$

An example of this algorithm is shown in Fig. 1 where fluid 1 is signed with the dark shade and the fluid 2 with the white one. The values of $f_{i+k,j+l}$ are known volume fractions of the fluid 1 in a 3×3 block of cells. The values of $f'_{i+k,j+l}(\vec{n})$ are the volume fractions (hatched area) due to the line with the normal $\vec{n}$ (dotted line in Fig. 1), which divides the block on two parts and conserves the volume fraction in the center cell of the block; i.e., $f_{i,j} = f'_{i,j}$. The LVIRA algorithm puts the interface segment between the boundaries of the cell (i, j) (thick black line in Fig. 1).

The second step in the interface tracking is the advection algorithm for the evolution of the volume fractions f in time. The volume fraction f follows the equation [23, 37]

$$\frac{\partial f}{\partial t} + \nabla \cdot (\vec{u} f) = 0. \tag{6}$$

Equation (6) reflects the fact that in an incompressible fluid the conservation of mass is equivalent to the conservation of volume and hence the conservation of f. The unsplit advection algorithm [37, 38] is used to calculate the temporal evolution of the volume fraction field f from Eq. (6).

The volume fraction function is used for the calculation of the fluid properties in the grid points, where both fluids are present:

$$\rho_{i,j} = f_{i,j}\rho_1 + (1 - f_{i,j})\rho_2. \tag{7}$$

$$\mu_{i,j} = f_{i,j}\mu_1 + (1 - f_{i,j})\mu_2. \tag{8}$$

The essence of the VOF model is to keep the interface sharp, which allows accurate location of the particular fluid and direct simulation of the eventual surface phenomena (surface

tension, phase-change, etc.). The accuracy of the model depends on the applied numerical scheme and on grid density. The model is not capable of simulating the phenomena with the scale smaller than the grid size.

3. THE TWO-FLUID MODEL

The two-fluid models are suitable for the two-phase problems, where the length scale of the interface shape is smaller than the grid size. The basic property of those models, that is, a consequence of the temporal and/or spatial averaging, is that each fluid as a continuum occupies the whole domain and therefore the interface is not calculated explicitly. Information lost by the averaging is replaced by more or less accurate closure relationships for the interfacial transfer of mass, momentum, and energy provided empirically mostly from experiments. This approach is more suitable for simulations of the dispersed flows; however, appropriate correlations also allow simulations of two-phase flow phenomena where the characteristic length of the interface is large compared to the grid size. The two-fluid models are usually designed for the simulations of the compressible two-phase flow [44], but in some cases, where the fluid velocities are small compared to the sound speed, the incompressible model is used [32]. Since the development of the coupling procedure between the two-fluid model and the interface tracking model is the main goal of this work, a very simple incompressible two-fluid model is chosen.

3.1. *Two-Fluid Model Equations*

The continuity and momentum equations for the system of incompressible viscous fluids used in the present model are [32]

$$\frac{\partial f_k}{\partial t} + \nabla \cdot (f_k \vec{u}_k) = 0, \tag{9}$$

$$f_k \rho_k \frac{\partial \vec{u}_k}{\partial t} + f_k \rho_k (\vec{u}_k \nabla)\vec{u}_k = f_k \rho_k \vec{g} - f_k \nabla p + C_k(\vec{u}_1 - \vec{u}_2) + f_k \nabla \cdot (\mu_k D_k). \tag{10}$$

The two-fluid system is described with two pairs of equations, (9) and (10), with $k = 1$ for fluid 1 and $k = 2$ for fluid 2. Both fluids are regarded as two mixed phases that share the same space and pressure and interact with the exchange of momentum (mass and energy transfer are not taken into account in Eqs. (9) and (10)). At any location there is a pair of velocities and volume fractions f_1 and f_2. Both fluids share space in proportion to their volume fraction, which satisfy the equation $f_1 + f_2 = 1$. The divergence free condition for the two-fluid model is provided by summation of Eq. (9) for $k = 1$ and Eq. (9) for $k = 2$ for both fluids

$$\nabla(f_1 \vec{u}_1) + \nabla(f_2 \vec{u}_2) = 0. \tag{11}$$

Since the volume fraction in the two-fluid model has a meaning similar to the color function (3) in the VOF model, the same symbol f is used. The momentum Eq. (10) for $k = 1$ and Eq. (10) for $k = 2$ are coupled with the third term on the right-hand side which is the inter-phase momentum exchange term due to a friction at the interface of the fluids. The interfacial friction depends on the flow regime of the two-phase flow. The coefficients C_1 and C_2 are given by [26]

$$C_1 = -C_2 = \frac{1}{8} c_d \rho_c a_i |\vec{v}_1 - \vec{v}_2|, \tag{12}$$

where ρ_c is a density of the continuous fluid, a_t is a volumetric interfacial area, and c_d is an empirical coefficient, which depends on the local Reynolds number and the flow regime.

A simplified interface friction coefficient, which is used in the present work is taken from the work of Mat and Ilegbusi [32]

$$C_1 = -C_2 = c_d \bar{\rho} f_1 f_2, \tag{13}$$

where $c_d = 20$ is an empirical constant and $\bar{\rho} = f_1\rho_1 + f_2\rho_2$ is the mixture density. The correlation (13) is applicable for laminar flows and small velocities and does not include the interfacial area variable a_i. More advanced two-fluid models use special correlations or even a special transport equation for a_i [34, 41], since it is a very important parameter for the calculation of all interface exchange terms. These models for a_i can be included without any essential change to the coupling model.

The two-fluid model is not so severely limited with the nodalization density as is the interface tracking model. Due to the averaged equations and corresponding closure relationships it can handle the phenomena on the smaller scale than the grid size. Of course the numerical scheme and nodalization density still affect the accuracy of the two-fluid model; however, the dominant contribution to the accuracy is the quality of the empirical correlations [44]. The main source of the uncertainty of the two-fluid models comes from the uncertainty of the correlations used to describe different flow regimes. Especially high uncertainties are usually experienced during transitions between different flow regimes.

4. COUPLED MODEL

The advantage of coupling the VOF and the two-fluid model is that some flow regimes with clear phase separation are not needed in the two-fluid model since they can be described more accurately by the VOF model. Because correlations are needed only for dispersed flows, coupling of these models improves the accuracy. On the other hand the coupled model with the inclusion of the two-fluid model prevents the non-physical interpretation of the dispersed flow by the VOF method.

The coupled model is designed to simulate the computational domain containing the area where the fluids are mixed and calculated with the two-fluid model (lighter gray area in Fig. 2) and the area where the fluids are separated and calculated with the VOF model (black and white areas in Fig. 2). During the simulation the two-fluid model area may change into the VOF area and vice versa. From the physical point of view the coupling is not problematic since both models use the same parameters to describe fluid flow. The advantage of the VOF model at coupling is that it uses the color function for tracking the interface, which has the same meaning as a volume fraction variable in the two-fluid model. The difference between the models is treatment of the fluid velocities. All the boundaries of the cell, which is in the two-fluid model domain, have two velocities obtained from Eq. (10)—one for each fluid. The remaining boundaries have only one velocity defined. When the model of the cell is changed, the velocities are redefined in order to conserve the volume flux. When the VOF model is changed to the two-fluid model, the velocities stay the same $\vec{u}_1^{\,two\text{-}fluid} = \vec{u}_2^{\,two\text{-}fluid} = \vec{u}^{\,VOF}$. But when the two-fluid model is changed to the VOF model the velocity is calculated as $\vec{u}^{\,VOF} = f_1\vec{u}_1^{\,two\text{-}fluid} + (1 - f_1)\vec{u}_2^{\,two\text{-}fluid}$.

Both sets of equations ((1), (2) and (10), (11)) were discretized and solved with the same numerical scheme due to the compatibility of model coupling. The numerical technique

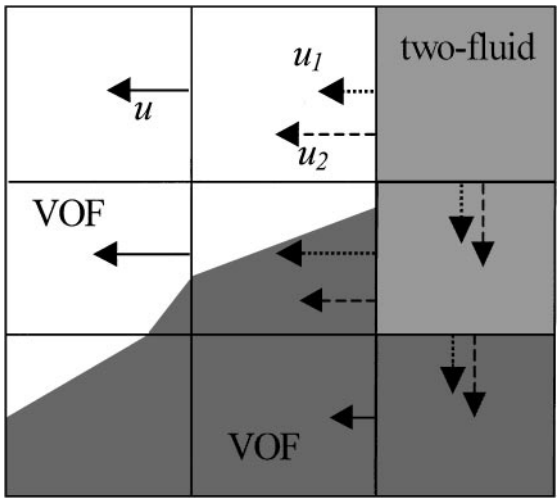

FIG. 2. Coupling of two-fluid and VOF area.

following the basic ideas of Rudman [39] was used to solve the time dependent incompressible Navier–Stokes equations on a staggered grid. The first-order algorithm for the time integration based on the projection method is used. The lower accuracy of the temporal integration is partially compensated for with the shorter time step, which did not exceed 0.1 fraction of the CFL time step. The Helmholtz equation for the pressure correction is solved with the biconjugate gradient method [16]. The second-order central differencing is used for spatial discretization of the convection terms with a proper amount of the upwind discretization, which reduces the numerical oscillations but does not reduce the accuracy order of the scheme.

The difference between the models is also the treatment of the volume fraction advection Eqs. (6) and (9). Equations (6) and (9) are in the same discretization form

$$f_{i,j}^{n+1} = f_{i,j}^{n} + \frac{\Delta t}{\Delta x}\left(H_{Xi-1/2,j} - H_{Xi+1/2,j}\right) + \frac{\Delta t}{\Delta x}\left(H_{Yi,j-1/2} - H_{Yi,j+1/2}\right). \qquad (14)$$

In Eq. (14) $H_{Xi+1/2,j}$ denotes the flux of volume fraction f across the right edge of the cell (i, j) and $H_{Yi,j+1/2}$ denotes the flux of f across the upper edge of the cell (i, j). Calculation of the flux H on the cell boundary depends on the cell, which is oriented upwind with the respect to the velocity. If the upwind cell is calculated with the VOF model, then the VOF advection algorithm is used (Fig. 3a); otherwise the two-fluid model is used to calculate the flux $H_{Xi+1/2,j}$ by the flux corrected transport algorithm [39] (Fig. 3b).

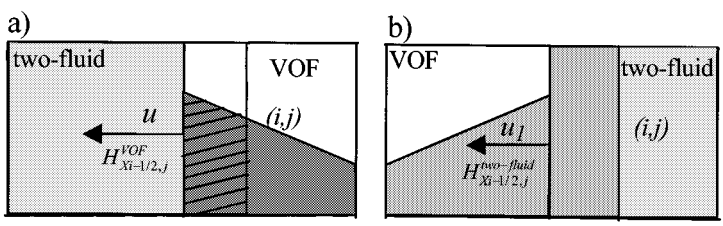

FIG. 3. Flux at coupling of two-fluid and VOF area. (a) Flux calculated by VOF model. (b) Flux calculated by "two-fluid" model.

5. SWITCH BETWEEN THE VOF AND THE TWO-FLUID MODEL

After the update of the volume fraction variable f, the VOF model or two-fluid model has to be assigned to each cell. The cells, which contain only one fluid, are automatically in the VOF domain. The essential problem of the coupling is a choice of a switch criterion. According to this criterion, the model that will be used in mixed cells, cells that contain both fluids, is chosen. The criterion must be based on the estimation of the local dispersion of the interface in the cell.

In our work the dispersion is estimated with the same function (5) that was used for the interface reconstruction. A dispersion function in the cell (i, j) is defined as

$$\gamma_{i,j} = \min(G_{i,j}(\vec{n})). \tag{15}$$

The function G defined by Eq. (5), which was originally developed for the calculation of the interface segment orientation $\vec{n}$ in the LVIRA interface reconstruction algorithm, turns out to be useful also for the estimation of the local dispersion. A dispersion function γ checks the positions of the fluids in the 3×3 block of cells with the respect to the best-estimated interface $\vec{n}$. The perfect non-dispersed state in the 3×3 block is achieved when the fluids are separated with the interface of the linear shape. In such a case the value of the dispersion function is zero; i.e., $\gamma = 0$. If a part of the fluid is located on the "wrong" side of the interface reconstucted by LVIRA algorithm, then $\gamma > 0$.

In order to couple the two-fluid model and the VOF model, a constant parameter γ_0 is required, such that

$$\begin{aligned} &\textit{if } \gamma_{i,j} < \gamma_0, \textit{ the interface in the cell (i, j) is reconstructed and the VOF model is used} \\ &\textit{if } \gamma_{i,j} > \gamma_0, \textit{ the fluids in the cell (i, j) are calculated with the two-fluid model.} \end{aligned} \tag{16}$$

The parameter γ_0 is a free input parameter of the model coupling. Setting γ_0 to the maximal possible value of dispersion γ means that the whole transient is calculated with the VOF method, whereas setting γ_0 to zero means no interface reconstruction and the two-fluid model is used the whole time on the whole domain.

5.1. *Transition from the VOF to the Two-Fluid Model*

In order to make the coupled model efficient the parameter γ_0 has to be determined properly. For that purpose it is necessary to estimate the upper bound of the dispersion γ and to analyze the behavior of γ in few typical two-phase systems, which are relevant to a given problem. The two-fluid state in the 3×3 block of cells can be very complex; therefore the characterstics of γ are determined numerically. Numerical tests with different physical phenomena [10–12] and simple numerical calculations on the 3×3 block have shown that the upper bound for the dispersion γ is $\gamma = 5$. Figure 4 shows an example of a system with the maximal dispersion $\gamma = 5$. The situation shown in Fig. 4 is rather unrealistic and never appears during the simulations of physical phenomena [12].

In order to estimate maximal values of γ in more realistic system, a homogenous mixture with $f(x, y, t) = f_{const}$ is considered first. The LVIRA interface reconstruction algorithm can be applied for such a system, despite the fact, that the reconstructed interface has nothing

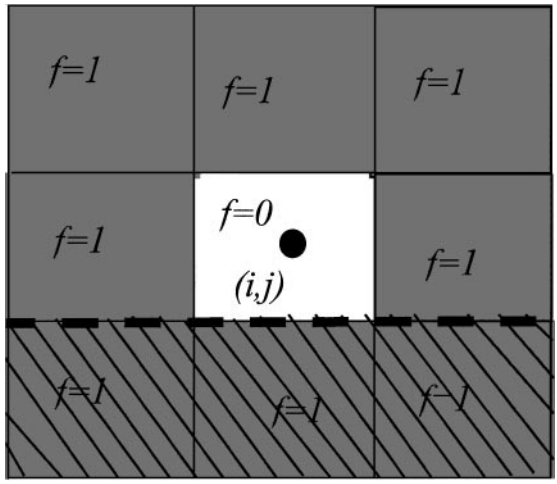

FIG. 4. Dispersion $\gamma = 5$ for the non-homogeneously dispersed fluids.

to do with the real physical picture. However, the resulting function γ defined by Eq. (15) can be used as a measure for the dispersion. Figure 5 shows the dispersion function γ of the homogeneous mixture as a function of the volume fraction f_{const}. The dispersion γ varies between $\gamma = 1.5$ and the maximal value $\gamma \cong 2$ at $f \cong 0.09$ (see Fig. 6). It turns out [12] that the maximal values of γ in realistic simulations are seldom higher than 2. Thus, in order to avoid the treatment of the homogenous mixture with the VOF model the switch parameter has to be limited to $\gamma_0 < 1.5$. However, the analysis of the dispersion in non-homogenous dispersed states with chunks larger than the grid size is required to obtain a more accurate value of γ_0.

Further analysis of the dispersion γ shows that it can be split into two parts:

I: Reconstruction of a single interface that cuts the 3×3 block of cells into two parts (see Fig. 1) results in a nonzero dispersion γ (15), when the interface is not linear in the 3×3 block.

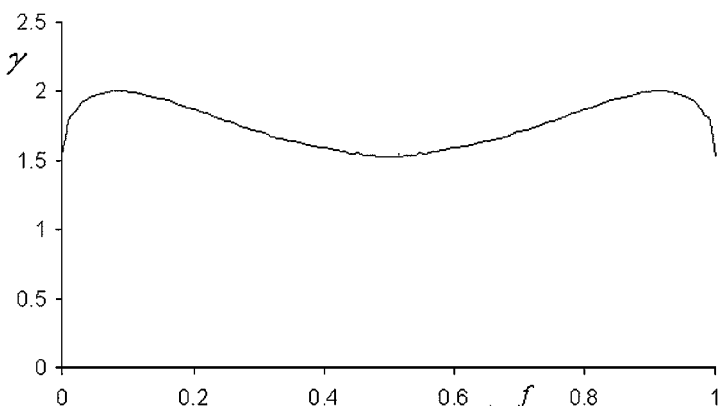

FIG. 5. Dispersion γ in the homogenous mixture as a function of volume fraction.

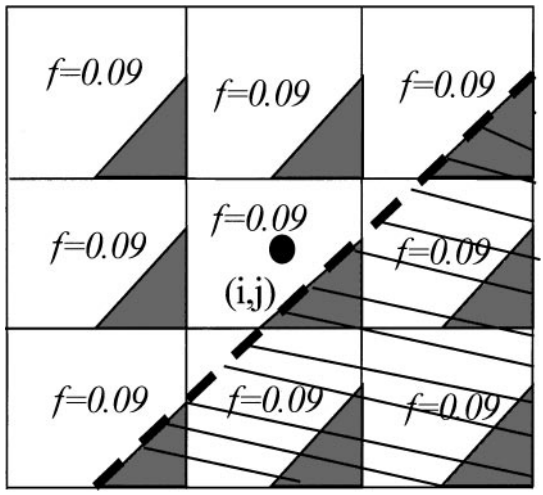

FIG. 6. Maximal dispersion $\gamma \cong 2$ of homogeneously dispersed fluids.

II: The second type of dispersion appears when two chunks (bubbles) of the dispersed fluid approach a distance smaller than the grid size.

Both parts of γ are analyzed in this section.

I. One of the most common topological shapes in two-phase flow is a bubble, which is used for the examination of the part I of dispersion γ. Figure 7 shows a circular bubble with a center in the point $S(x, y)$ and diameter d on a mesh with the grid spacing h. The maximal dispersion calculated in any of the cells covered by the bubble interface is denoted as γ_M. All relative positions of the bubble were checked numerically by moving the center of the circle S within a single cell (Fig. 7, hatched area). Figure 8 shows the maximal dispersion γ_M for different bubble positions. The result in Fig. 8 shows that using γ as a measure of the interface dispersion gives values, which depend on the position of the interface in the discrete grid. An ideal parameter for measuring the dispersion should have a constant value for all

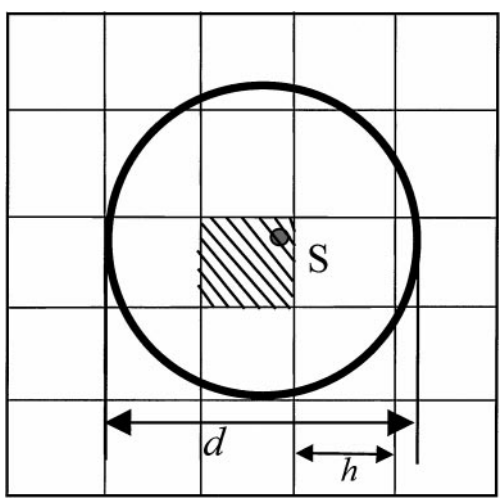

FIG. 7. Position of a circular bubble on a grid.

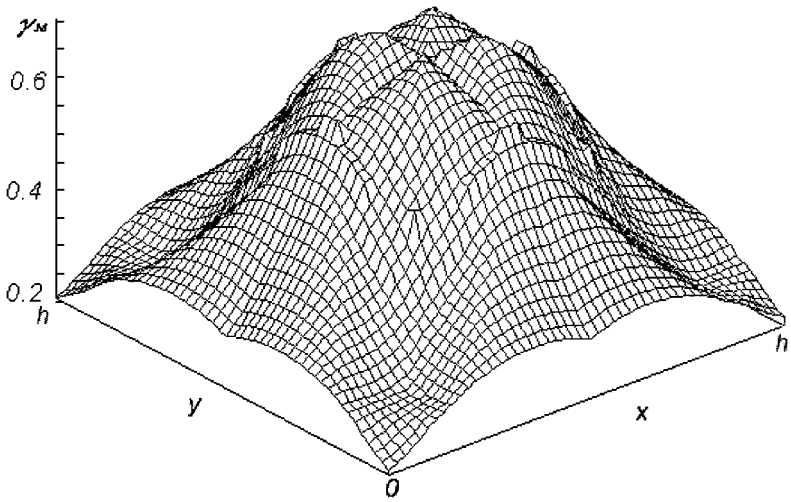

FIG. 8. Maximal dispersion γ_M for circular bubble with $d/h = 3.8$.

positions of the bubble; however, it is probably impossible to construct such a parameter. More detailed behavior of the dispersion γ is given in Fig. 9, where $\gamma_{min} = \min(\gamma_M(x, y))$ and $\gamma_{max} = \max(\gamma_M(x, y))$ are given as functions of the bubble diameter to cell length ratio d/h. A larger d/h ratio means more grid cells per bubble and results in smaller values of the dispersion γ. Figure 9 shows a rapid increase of γ values for diameters d less than approximately $2h$ to $3h$. This result shows that at least three grid cells per bubble diameter are needed to capture its circular shape with some minimal accuracy and justifies the choice of γ as a measure of the interface dispersion.

The result in Fig. 9 allows us to set a new threshold value γ_0: setting $\gamma_0 = \gamma_{max}$ determines the minimal characteristic size of the bubble, which can be simulated with the VOF method. For example, setting $\gamma_0 = 0.6$ means that the bubble or a part of the surface with the characteristic size $d > 4h$ are treated with the VOF model. Smaller chunks with dispersion

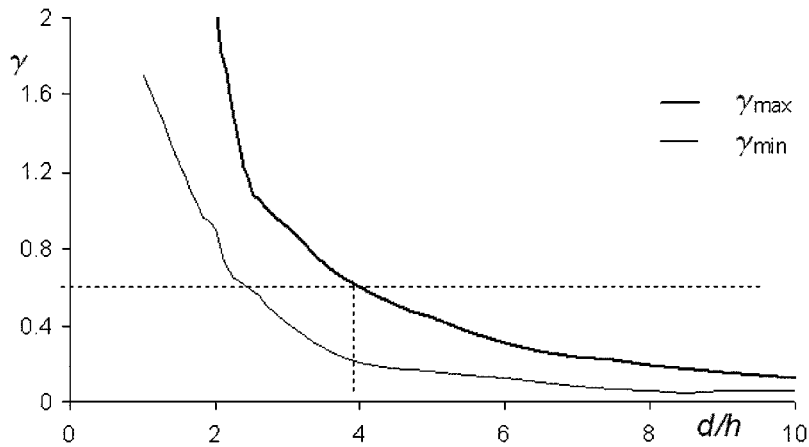

FIG. 9. Dependence of the dispersion parameters from the bubble diameter.

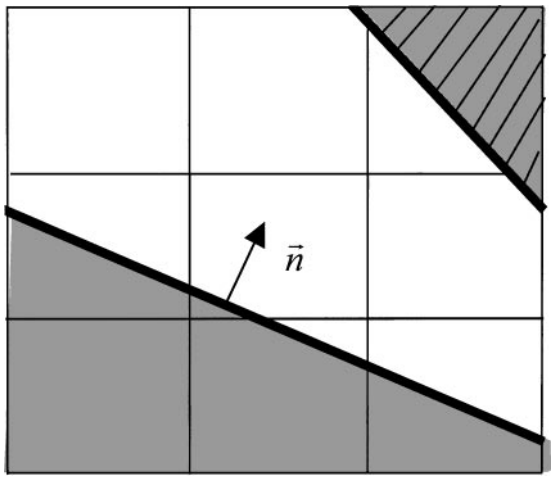

FIG. 10. Part IIa dispersion due to the nearby interfaces.

$\gamma_{max} > \gamma_0$ and $\gamma_{min} < \gamma_0$ might be still treated with the VOF model, but as such chunks move over the discrete grid, the dispersion in some cell on the interface sooner or later exceeds the parameter value γ_0 and switches the cell to the two-fluid model.

II. If two chunks of fluid approach each other at a distance comparable to the grid spacing, γ will grow and the two-fluid model will be switched on. This type of dispersion is named part II dispersion and is shown in Figs. 10 and 11. The original volume fraction is signed with gray color and the reconstructed interface is presented with the thick line. The hatched area covers the mesh cells, which contribute to the dispersion in the center cell $\gamma_{i,j}$. Due to the linear interfaces there is no part I dispersion in Figs. 10 and 11, but only the part II dispersion due to the presence of the nearby interface appears. There are two kinds of part II dispersion:

IIa: Nearby interface enlarges the γ value, but does not disturb the reconstruction (Fig. 10).

IIb: Nearby interface is so close that the reconstruction fails (Fig. 11).

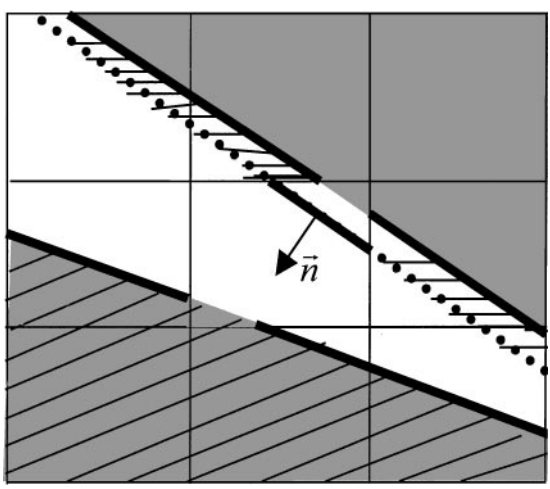

FIG. 11. Part IIb dispersion–reconstruction error due to the LVIRA failure.

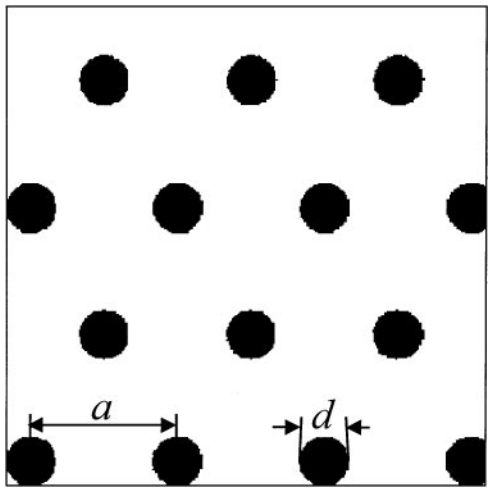

FIG. 12. Homogenous distribution of bubbles with $d/h = 3$.

The analysis of the dispersion due to the interface contact is needed to determine the relation between the threshold γ_0 and the failed reconstruction. The VOF model should not treat the state, where the reconstruction failure appears. Due to the numerous combinations of states, where two interfaces come into the contact in the 3×3 block of cells, the part II dispersion analysis was performed statistically.

The dispersion γ from Eq. (15) cannot distinguish the dispersion cases IIa and IIb. The reconstruction error IIb can only be detected by comparison with the exact solution. Thus the part II dispersion was analyzed in the homogenous mixture of constant diameter bubbles shown in Fig. 12. For that purpose the following expression based on the volume fraction difference is used to measure the reconstruction error

$$\delta = \frac{1}{V_1} \int_V (f_{exact} - f_{rec})^2 \, dV. \tag{17}$$

The reconstruction error is denoted with δ, f_{exact} is the exact volume fraction function that is known in advance, f_{rec} is the approximation of the original state obtained with the LVIRA reconstruction algorithm, V is the computational domain, and $V_1 = \int_V f_{exact} \, dV$ is the volume of the dispersed phase used as a normalization factor. $\delta = 0$ means that the reconstruction is absolutely correct. $\delta > 0$ is caused by a linear reconstruction of the curved interface and/or failed reconstruction of the interface that corresponds to the part IIb dispersion. The expression (17) compares particular cells without their local surrounding (unlike dispersion (15)); therefore it does not detect the part IIa dispersion due to the nearby interface.

In order to compare the dispersion γ and reconstruction error δ, the average dispersion is defined as

$$\bar{\gamma} = \frac{\sum_i \sum_j \gamma_{i,j}}{N}. \tag{18}$$

It is calculated on the whole domain, where N is a number of the cells, which contain both fluids.

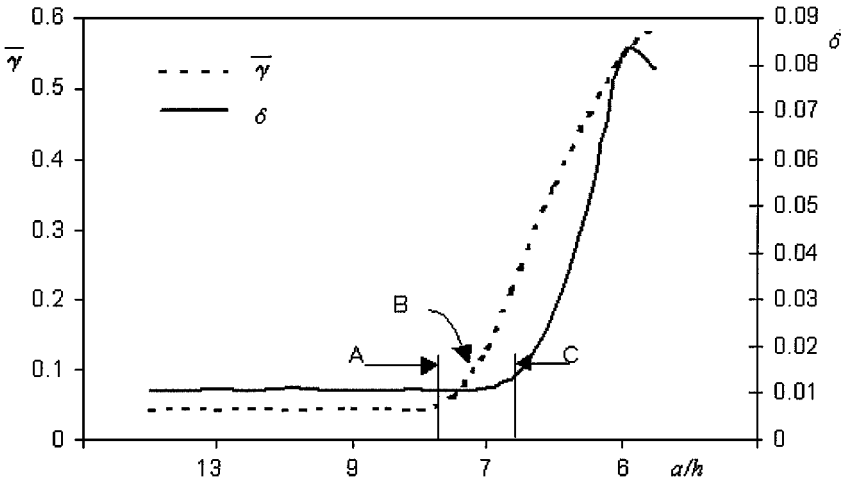

FIG. 13. Comparison of dispersion and reconstruction error at $d/h = 3$.

The comparison of the average dispersion $\bar{\gamma}$ and the reconstruction error δ can distinguish dispersion parts IIa and IIb. Figure 13 compares δ and $\bar{\gamma}$ for the state of the uniform bubble mixture as a function of the bubble density—a/h ratio at a constant d/h ratio. The constant values of the functions $\bar{\gamma}$ and δ at large a/h ratios (part A in Fig. 13) are due to the linear approximations of the curved interfaces, which depend only on the size of the bubbles (d/h ratio). In part B the dispersion $\bar{\gamma}$ is enlarged due to the presence of the nearby interface but the reconstruction does not fail yet (example in Fig. 10), since reconstruction error δ is not enlarged. The part C in Fig. 13 is the area where the LVIRA reconstruction algorithm fails (example in Fig. 11).

The goal of this procedure is to estimate of the reconstruction error IIb with the dispersion function γ and to impose additional constraints on the threshold parameter γ_0. The area where γ is larger than the threshold value γ_0 is in the two-fluid model domain and in that case the interface is not reconstructed. When calculating the reconstruction error δ in the coupled model that area is excluded from the δ:

$$\delta(\gamma_0) = \frac{1}{V_1} \int_{V_{\gamma<\gamma_0}} (f_{exact} - f_{rec})^2 \, dV. \tag{19}$$

Figure 14 shows the dependence of $\delta(\gamma_0)$ on the a/h ratio at a constant bubble diameter $d/h = 3$ for the system shown in Fig. 12. The smaller γ_0 parameter reduces the reconstruction error $\delta(\gamma_0)$ since a larger portion of the area with failed interface is excluded from the integration domain in Eq. (19). If the interfaces of the structures are so close that the reconstruction fails, that area should be detected by the dispersion criterion and excluded from the integration (19). Figure 14 shows that for the case of uniform bubble mixture at $d/h = 3$, γ_0 should not exceed the number of approximately $\gamma_0 \approx 0.8$. For larger values of γ_0, the areas with failed interface reconstruction can be erroneously treated with the VOF method. In general this assumption defines the γ_{rec} parameter, which in the case $\gamma_0 = \gamma_{rec}$ excludes the area with failed reconstruction. In that case the reconstruction error $\delta(\gamma_{rec})$ (Fig. 14) does not increase when the a/h ratio is decreased. Calculations shown in Fig. 14 were repeated for different d/h ratios and γ_{rec} as a function of the bubble diameter d/h was

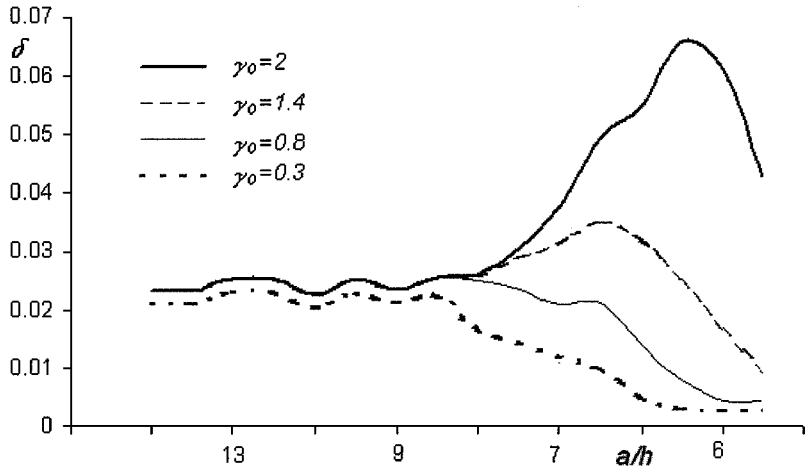

FIG. 14. Reconstruction error for different values of switch parameter γ_0 at $d/h = 3$.

obtained. It is presented in Fig. 15. According to the γ_{rec} in Fig. 15, setting $\gamma_0 \lesssim 0.4$ ensures that almost every cell with the reconstruction error of type IIb switches to the two-fluid model. On the basis of the numerical experiments, a larger value $\gamma_0 = 0.6$ was chosen in this work. That allows some reconstruction error for the chunks larger than approximately $d/h > 6$. This choice is justified by the physical picture of the phenomena: when two such large chunks approach it is often more sensible and accurate to keep the simulation with the VOF method and allow some reconstruction error at merging, than switching to the less accurate two-fluid model, which cannot improve the prediction of the merging process.

5.2. *Transition from the Two-Fluid to the VOF Model*

Stratification of mixed fluids is the reverse process of the dispersion. The transition from the VOF to the two-fluid model depends on the interface position and distortion. The

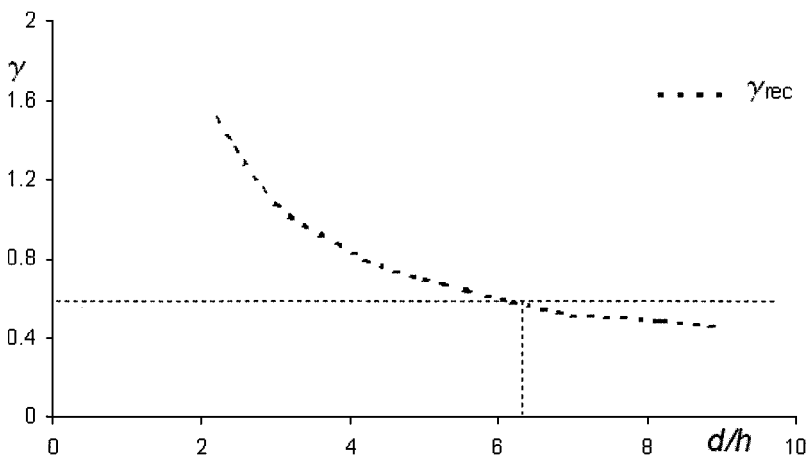

FIG. 15. Dependence of the γ_{rec} parameter from the bubble diameter.

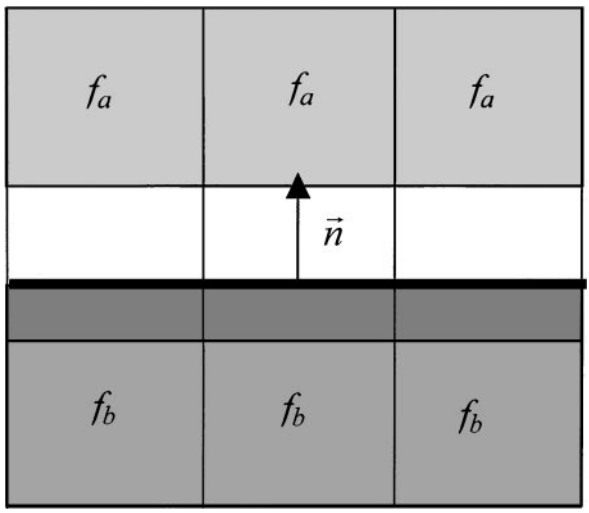

FIG. 16. Setting interface at the stratification process.

reverse process is more complex since the more accurate VOF model has to be activated from the results of the less accurate two-fluid model. Additional empirical correlations may be required in some two-fluid models to describe such a transition. Besides the volume fractions, these correlations may include also other variables such as a relative velocity between fluids. It turns out that the dispersion γ with $\gamma_0 = 0.6$ can be used as a simple model of transition from the two-fluid to the VOF model. The results show that this is a successful approximation in the presented case.

In the simplest case, when homogeneously dispersed fluids are separating in a vertical direction, the coupled model sets up the interface horizontally as shown in Fig. 16. The upper cells indicated with the lighter gray area contain smaller volume fraction of the heavier fluid f_a than the bottom cells $f_b > f_a$. Despite the fact that the system is dispersed and treated with the two-fluid model equations, the LVIRA algorithm is applied in each cell in order to obtain the dispersion γ. The stratification appears in the cells with $\gamma < \gamma_0$, where the VOF model sets up the interface. In the simple case shown in Fig. 16, the interface is located in all three middle cells due to the homogeneity of the problem in the horizontal direction. In that case the relation between the values f_a and f_b, at which the interface is reestablished, can be calculated from the simplified Eq. (15):

$$\gamma = 3f_a^2 + 3(1 - f_b)^2 < \gamma_0 \Rightarrow f_a < \left(\frac{\gamma_0}{3} - (1 - f_b)^2\right)^{1/2}. \tag{20}$$

Figure 17 shows the area of values f_a and f_b, where the interface is set up during the stratification process for two different values of γ_0.

The necessary (but not sufficient) condition for the interface reestablishment is $f_a < 0.5$ and $f_b > 0.5$ (or $f_a > 0.5$ and $f_b < 0.5$); i.e., the interface can be established only between the mixture of bubbles and the mixture of droplets. This is a consequence of the physical/geometrical property that bubbles or/and droplets cannot exist if the continuous fluid has a void fraction $f_{cont} < 0.5$ [6]. In the case when volume fractions f_a, $f_b < 0.5$, the threshold γ_0 has to be smaller than the minimal possible dispersion to avoid the construction

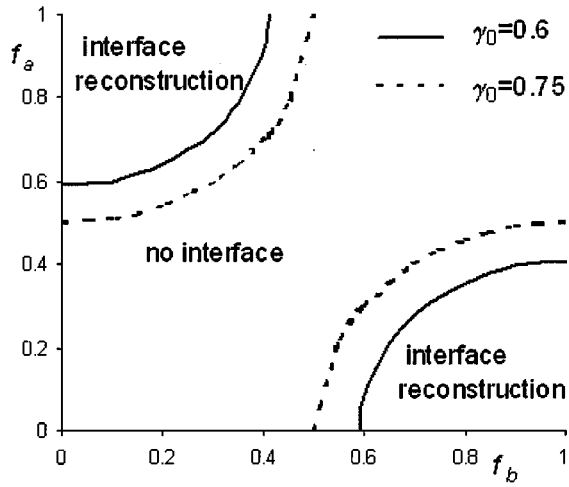

FIG. 17. Ratio of volume fractions f_a and f_b at the point of interface setup.

of the interface

$$f_a,\ f_b < 0.5 \Rightarrow \gamma_0 < \min\left(3f_a^2 + 3(1 - f_b)^2\right) = 0.75. \tag{21}$$

Due to the symmetry of the void fractions, the same limit for γ_0 is obtained for $f_b,\ f_a > 0.5$. Values different from 0.75 are obtained for stratification in directions that are not parallel to the discrete grid, or for a general stratification. However, the differences are small.

According to the results of the calculations summarized in Figs. 9, 15, and 17, $\gamma_0 = 0.6$ was used as a value of the threshold parameter γ_0. This value gives the following properties of the coupled model:

(1) The chunks with the characteristic size $d > 4h$ are treated with the VOF model. The surface of the smaller chunks is at least partially assigned to the two-fluid model.

(2) The reconstruction error can appear in the VOF model when the chunks with $d > 6h$ approach each other.

(3) The stratification cannot be activated, when the continuous volume fraction is $f_{cont} < 0.6$. Larger values of γ_0 allow smaller structures and therefore less accurate reconstruction of the interface, while smaller values activate the two-fluid model in the areas where the VOF model is still accurate.

6. RESULTS

For testing the coupled model two different examples were chosen. The idealized example of the vortex flow [38] was used to show the behavior of the coupling algorithm with advection and vorticity. The second simulation of the Rayleigh–Taylor instability shows the capability of the coupled model at the physical problem.

6.1. *Simulation of the Vortex Flow*

For the overall estimation of the reconstruction error a test problem with the topological changes of the interface is needed. The two-dimensional test problem, that besides the

topology change is also easy to implement, is the vortical flow test proposed by Rider and Kothe [38]. Such test is representative of the interfacial flow in the real physical systems such as the Rayleigh–Taylor instability where the sharp gradients in the fluid properties lead the transient mechanisms. This test was used in [38] and [48] for estimating the accuracy of the particular reconstruction algorithms and for comparison to the other reconstructing algorithms.

The vortical flow test uses a fixed velocity field defined by the stream function:

$$\Psi = \frac{1}{\pi} \sin^2(\pi x) \sin^2(\pi y) \tag{22}$$

The initial state of the fluid 1 is a circle with the radius $r = 0.07$ whose center is located at the point $S(0.5, 0.87)$ (Fig. 18). The vortical velocity defined by (22) deforms the circle into the curved stripe. Figure 19 shows the state at $t = 1.6$ calculated with the VOF model on the 224×224 grid. This is the maximal time, where the VOF method is capable of fully resolving the state on the 224×224 grid. Theoretically the fluid structure during the rotation makes a spiral of the thin stripe, which stays continuous even in the case of infinite whirling $t \to \infty$. During the simulation when the thickness of the fluid is close to the grid size the numerical dispersion occurs. The original stripe decays into several parts comparable to the grid size as shown in Fig. 20. Figure 21 shows the same state simulated with the coupled model, where the volume fraction field is presented with gray casts. Since the two-fluid model is involved in the calculation, the result is affected by numerical diffusion. However, this solution is still closer to the real world than the solution in Fig. 20. To evaluate the correctness of this particular simulation approach we compare the volume fractions f with the "correct" solution by

$$\delta_{nod}(t) = \frac{1}{V_1} \sum_{(i,j)\in V} (f_{grid\,A}(t) - f_{grid\,B}(t))^2_{i,j}, \tag{23}$$

where $f_{grid\,A}$ is a volume fraction field calculated on a coarser grid, $f_{grid\,B}$ is a volume fraction calculated on a finer grid (Fig. 19) and interpolated on the coarser grid A, and V_1 is a volume of the fluid 1 $V_1 = \sum f_{grid\,A}$. In our case the result on grid $B = 224 \times 224$ is used

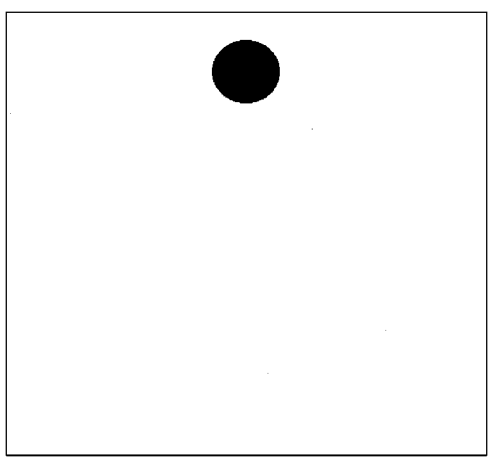

FIG. 18. Initial state of the vortex flow test.

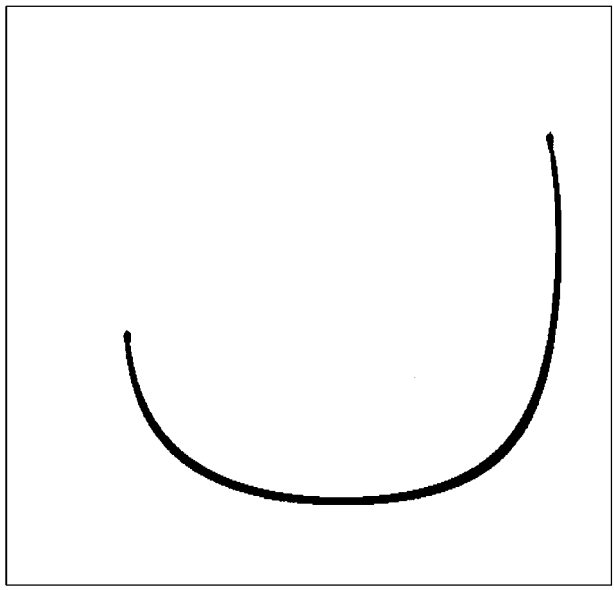

FIG. 19. Solution of the vortex flow test at $t = 1.6$ calculated on 224×224 grid with the VOF model.

as a "correct" solution. In Fig. 22 the $\delta(t)$ for different mesh density and different models are compared. The error $\delta(t)$ is close to zero till the numerical dispersion occurs. On the mesh 28×28 that happens at $t = 0.75$ and on 56×56 at $t = 1.2$. After that the numerical surface tension enlarges the error of the VOF model simulation, while the numerical diffusion affects the result of the coupled (two-fluid) model. The change of $\delta(t)$ is more rapid at the VOF

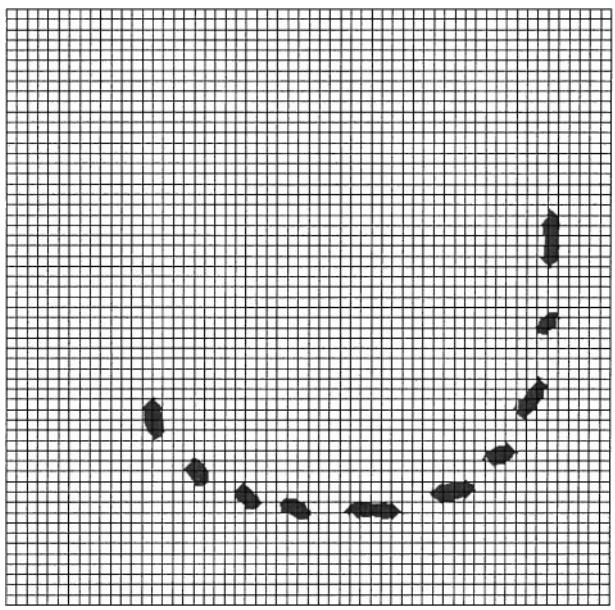

FIG. 20. Solution of the vortex flow test at $t = 1.6$ calculated on 56×56 grid with the VOF model.

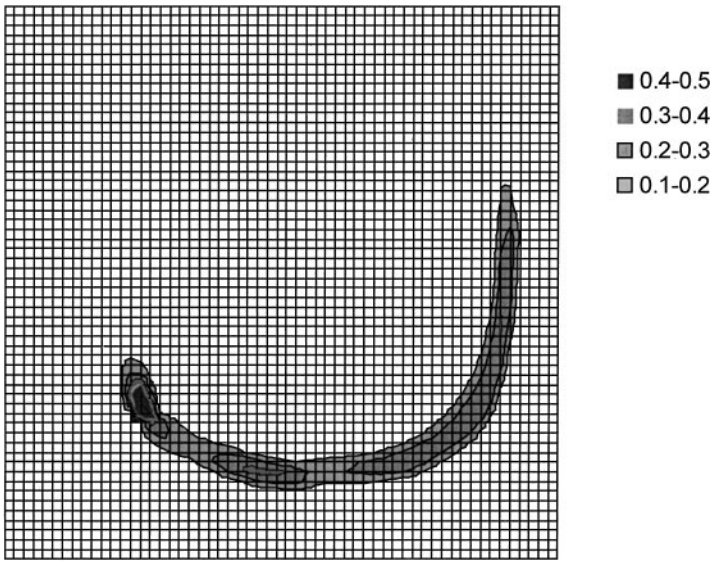

FIG. 21. Solution of the vortex flow test at $t = 1.6$ calculated on 56×56 grid with the coupled model.

model since the numerical surface tension disperses the fluids in a relatively short time interval. On the other hand the numerical diffusion of the two-fluid model enlarges the error more continuously.

A better numerical scheme would improve the results of the two-fluid and the coupled models; however, it cannot avoid the numerical surface tension effect.

6.2. *Simulation of the Rayleigh–Taylor Instability*

The only true evaluation of the coupled model is a comparison to the corresponding experiment. A comparison of results obtained with the coupled model and the real experimental data is possible only partially: like the numerical methods, which are designed for the simulations of the dispersed or stratified flow, the experiments are also specialized for

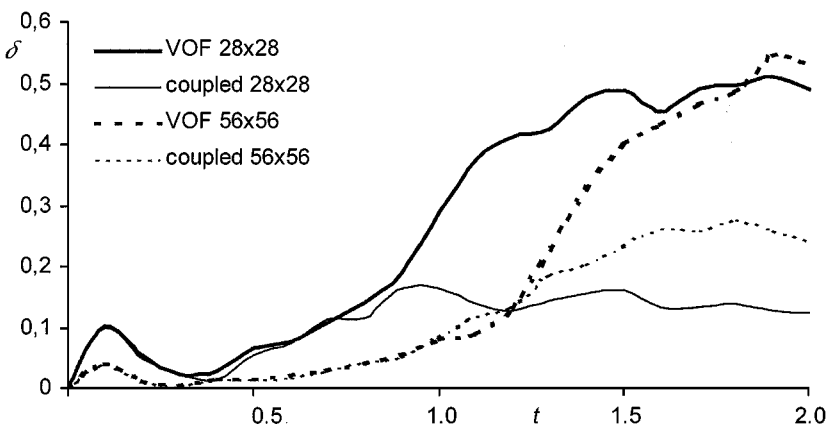

FIG. 22. Time development of $\delta(t)$ for the vortex flow test from $t = 0$ to $t = 2$.

the examination of a particular flow type. Among the basic two-phase flow phenomena such as the Kelvin–Helmholtz instability [35] and the bubble stability [43], the Rayleigh–Taylor instability turns out to be the most suitable for the assessment of the coupled model, since during the transient the two-phase flow changes from stratified to dispersed and vice versa. Besides that, the Rayleigh–Taylor instability has been examined with numerous calculations and serves as a kind of benchmark test for novelties in the two-phase flow modeling. A similar work to our study has been performed by Glimm and co-authors, where the mixing zone at Rayleigh–Taylor instability was examined [18]. That study combined the front tracking method with the statistical model [17] to handle the late nonlinear and chaotic stage of the Rayleigh–Taylor instability. In our work, the numerical simulations with different grid densities were performed to point out the capability of the coupled model to handle the dispersion problem with some limited accuracy even on a coarse grid.

In the initial state of the phenomenon, the heavier fluid $\rho_1 = 3$ lies above the lighter one $\rho_2 = 1$ in a channel with the width 1 and height 5. The sinusoidal disturbance of the interface with the amplitude 0.002 is increased due to gravity acceleration $g = 10$. Both fluids have the same kinematic viscosity $v_1 = v_2 = 10^{-2}$. All quantities mentioned above are nondimensional.

Figures 23 and 24 show the VOF simulation performed with different grid densities. The heavier fluid is marked with balck and the lighter fluid is white. Figure 23 shows that the VOF method successfully resolves the instability on the grid 48×240 or denser until $t \approx 2$. Further development of the phenomenon mixes the fluids to the dispersed state,

FIG. 23. State of the Rayleigh–Taylor instability at time $t = 2.0$ simulated with the pure VOF method.

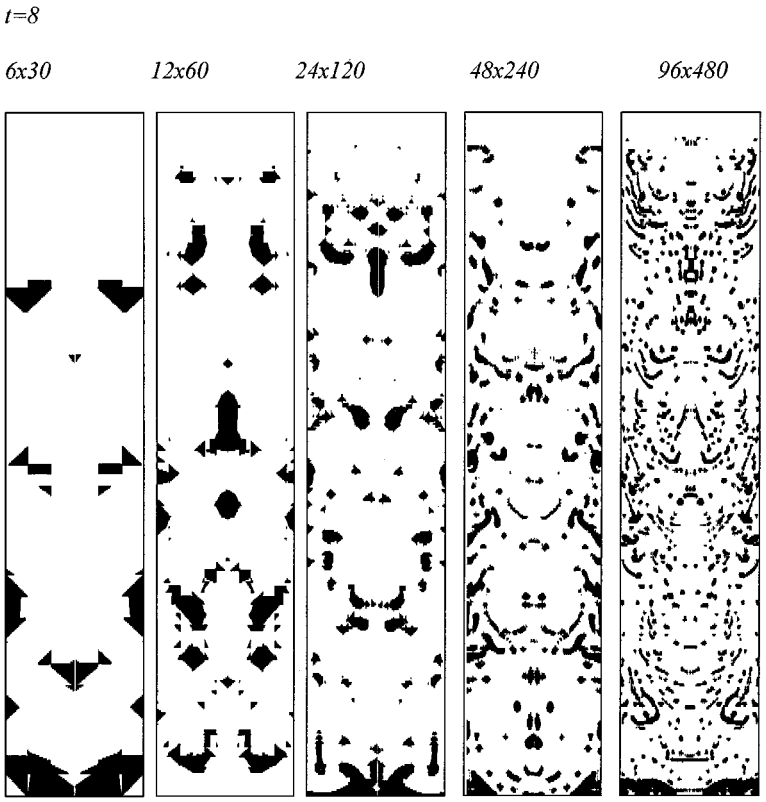

FIG. 24. State of the Rayleigh–Taylor instability at time and $t = 8.0$ with the pure VOF method.

because there is no force like a surface tension, which would limit the dispersion. A denser and denser grid is needed to resolve the continuation of the transient. For example, the dispersed state like the one at $t \approx 8$ in Fig. 24 shows a different distribution of fluids for every nodalization. Such a state is far beyond the capabilities of the 96×480 mesh and our computer hardware.

The grid dependence is investigated in the same way as Eq. (23), as in the vortical flow test. Figure 25 shows the temporal development of the $\delta_{nod}(t)$ function for several pairs of grids. In the initial phase of the transient higher resolution gives more accurate results (lower δ_{nod}) since the reconstruction errors appear later. However, after a certain time interval, when the fluids are well mixed, all VOF simulations end with unacceptable reconstruction errors. The VOF method numerically disperses the fluids on small chunks, whose size depends on grid density—denser nodalization produces smaller chunks. Their motion is significantly affected by the reconstruction error and is not physical. "Numerical" chunks on a denser grid moves slower and therefore the volume fraction distribution and $\delta_{nod}(t)$ significantly depends on the grid density at the sedimentation part of the transient.

Figure 26 shows one of the initial stages simulated with the coupled model using different grid densities. The black and white areas denote the position of the heavier and lighter fluid, respectively, while the two-fluid mixture is presented with gray casts. Larger volume fraction of the heavier fluid (larger f) is presented with darker cast. The finer grid is capable of simulating smaller structures before the two-fluid model is activated. Therefore at higher resolution a smaller area is calculated with the two-fluid model (gray area in Fig. 26). The

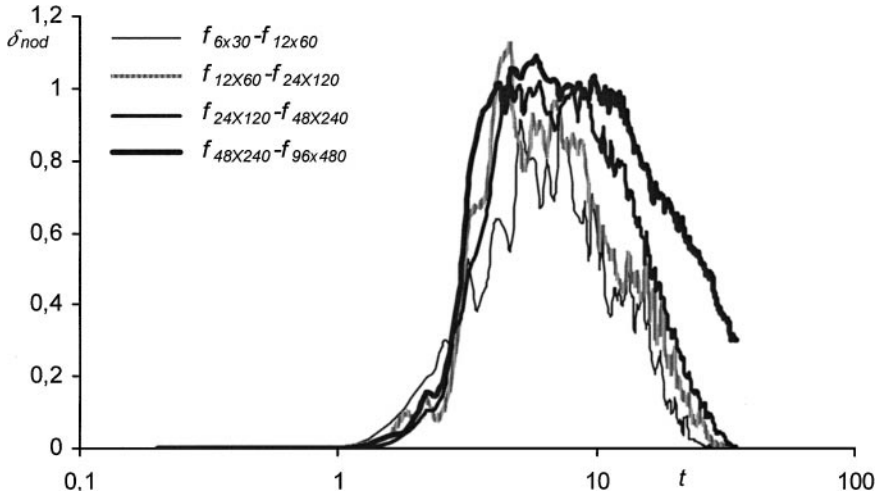

FIG. 25. Convergence of VOF model.

two-fluid model is first activated on the part of the interface with the smallest characteristic size (gray area in Fig. 26 at finest resolution). After that it is spread around due to the further fluid motion and also due to the numerical diffusion, which affects the volume fraction field in the two-fluid model.

FIG. 26. Grid dependence of the coupled model showed on the state at $t = 2.0$.

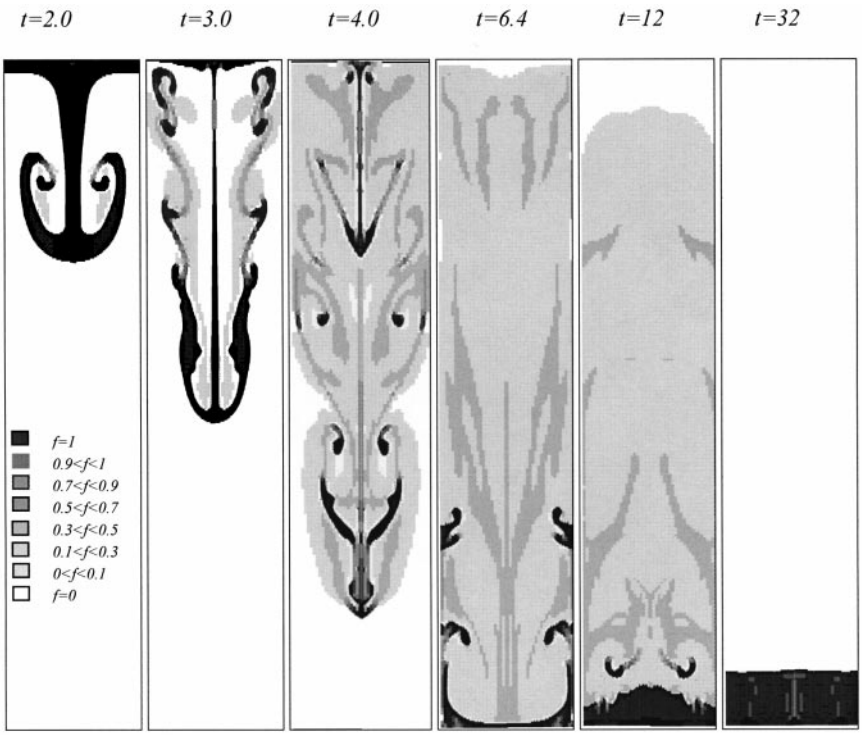

FIG. 27. Time development of the instability simulated with the coupled model on 48 × 240 grid.

Figure 27 shows the time development of the instability simulated with the coupled model. At the initial stages of the transient the VOF model is used. Once the two-fluid model is activated, it is spread all over the calculation domain due to the vortices, which appear during the transient. In the final stages of the transient, mixing of the fluids is replaced by the stratification process, which leads to the reverse process—construction of the new interface and activation of the VOF model between the lighter and the heavier fluid. Mixing and stratification processes are described by the two-fluid model and depend mainly on the empirical constant for the interfacial friction c_d.

The interfacial friction constant c_d should be evaluated in order to describe the real physical picture as close as possible. Since the correct solution of the problem is not known and there is a lack of experiments, which would give appropriate data, the evaluation appeared to be a rather difficult task. Therefore the simulation of the Rayleigh–Taylor instability with the pure VOF model was used as a reference solution to determine c_d. Although this bulk solution is not accurate, it is used for comparison with the coupled model. Since the simulation with the pure VOF model is grid dependent, only the result on the 48 × 240 mesh density is used for the valuation of the interfacial friction, which is set to $c_d = 40$ to match the bulk solution as close as possible.

The characteristics of the coupled model are showed similarly as pure VOF model in Fig. 25 by comparing the volume fraction distributions of different resolutions with the Eq. (23). Figure 28 shows $\delta_{nod}(t)$ of the coupled model for several pairs of grids. The δ_{nod} stays low when the same model is used on both grids (VOF model at the beginning and two-fluid model at the end of the simulation). The peak δ_{nod} occurs at switching from VOF

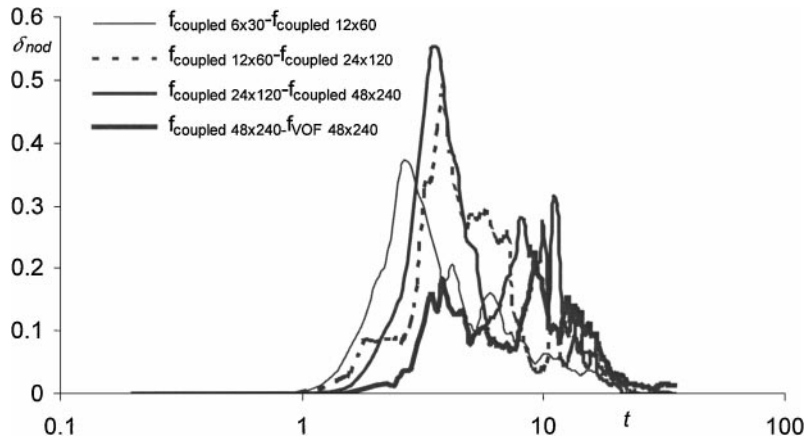

FIG. 28. Convergence of the coupled model.

to two-fluid model. The switch is grid dependent and on denser resolution it turns on later. The peak in $\delta_{nod}(t)$ describes the part of the transient when the two-fluid model on the coarser grid has already been switched on, while the VOF model still works on the finer grid.

For the initial part of the transient ($t < 2$) denser grids give lower $\delta_{nod}(t)$ because the coupled model uses the VOF model, which is capable of simulating that part and is not affected by the reconstruction error. Later ($t > 5$), when the fluids disperse, $\delta_{nod}(t)$ is much smaller than that in the VOF model (Fig. 25) for all grid densities. The distribution of the volume fraction in the second part of the transient ($t > 5$) is driven by the two-fluid model and depends mainly on the interfacial friction constant. On the other hand the volume fraction distribution in the pure VOF model appeared to depend also on the grid density.

Since the parameters $\delta_{nod}(t)$ of the coupled model in Fig. 28 are approximately the same as $\delta_{nod}(t)$ of the bulk solution and are much lower than $\delta_{nod}(t)$ of the pure VOF model, we confirmed the low grid dependence of the coupled model. With the inclusion of the two-fluid model the coupled model becomes less grid dependent and is able to simulate the problem on the coarsest grid more correctly than the pure VOF model on the highest resolution.

7. CONCLUSIONS

The coupling of a simple VOF model and a two-fluid model was proposed and used for the simulation of the two-phase problem with the dispersion of the interface. The interface tracking algorithms such as the VOF method are useful for the simulation of the initial part of the phenomenon. But further development of the instability is beyond the capabilities of the interface tracking algorithms, which are limited by the grid size. The addition of the two-fluid model to the model with the VOF method eliminated this problem and enabled the simulation of the whole phenomenon without the restriction imposed by the grid density.

The coupled model exploits particular characteristics of both models: accurate simulation of the interface with the VOF model and relatively small grid dependence of the two-fluid

model in the dispersed flow. The switch parameter between the models is provided from the function, which is already used by the LVIRA interface reconstruction algorithm in the VOF method. Some simple numerical calculations have shown that the switch parameter γ_0 between 0.4 and 0.6 is the most proper value to change from the VOF to the two-fluid model and vice versa. This value disables the interface reconstruction of the chunks with the characteristic size close to the grid size and smaller and replaces it with the two-fluid model. The switch between the models is based only on the position of the volume fractions, and can be upgraded for more complex transients with other parameters and empirical correlations.

The coupled model gives results, which are grid dependent; i.e., a denser nodalization does not result in a grid independent solution, but it gives a better approximation. The simulation of the coupled model with the lower nodalization gives qualitatively the same result as on the higher resolution but with a larger error.

The vortex flow test and simulation of the whole transient of the Rayleigh–Taylor instability, until the fluids exchange their positions, has showed that the coupled model of the VOF model and the two-fluid model enables a more realistic calculation of a wider range of two-phase phenomena than the pure VOF model. Comparison of the coupled model with experimental models is difficult since there are not many experiments investigating both the interface tracking and the dispersion phenomena at the same time.

REFERENCES

1. J. U. Brackbill, D. B. Kothe, and H. M. Ruppel, FLIP: A low-dissipation, particle-in-cell method for fluid flow, *Comput. Phys. Comm.* **48**, 25 (1988).
2. J. U. Brackbill, D. B. Kothe, and C. Zemach, A continuum method for modelling surface tension, *J. Comput. Phys.* **100**, 335 (1992).
3. J. D. Bugg, K. Mack, and K. S. Rezkallah, A numerical model of Taylor bubbles rising through stagnant liquids in vertical tubes, *Int. J. Multiphas. Flow* **24**, No. 2, 271 (1998).
4. M. Bottoni and W. Sengpiel, *Review of Mathematical and Physical Basis of Two-Phase Flow Modelling*, KFK report (Institut fùr Reaktorsicherheit, Kernforschungszentrum, Karlsruhe, 1992).
5. B. Bunner and G. Tryggvason, Direct numerical simulation of three-dimensional bubbly flows, *Phys. Fluids Lett.* **11**, No. 8, 1967 (1999).
6. K. E. Carlson, R. A. Riemke, S. Z. Rouhani, R. W. Shumway, and W. L. Weaver, *RELAP5/MOD3 Code Manual, Models and Correlations* (EG&G Idaho, Idaho Falls, 1991), Vol. 4, FIN No. A6052.
7. S. Chandrasekhar, *Hydrodynamic and Hydromagnetic Stability* (Oxford Univ. Press, London, 1961).
8. L. Chen, S. V. Garimella, J. A. Reizes, and E. Leonardi, The development of a bubble rising in a viscous liquid, *J. Fluid Mech.* **387**, 61 (1999).
9. C. T. Crowe, M. Sommerfeld, and Y. Tsuji, *Multiphase Flow with Droplets and Particles* (CRC Press, Boca Raton, Florida, 1998).
10. G. Černe and S. Petelin, Simulation of the bubble motion with the interface tracking method, in *Proceedings of the 3rd ASME/JSME Joint Fluid Engineering Conference*, FEDSM99-7089 (1999).
11. G. Černe and S. Petelin, Simulation of the Kelvin–Helmholtz instability with the volume of fluid method, in *Proceedings of 9th International Topical Meeting on Nuclear Reactor Thermal Hydraulics (NURETH-9)* (1999).
12. G. Černe, S. Petelin, and I. Tiselj, Simulation of the instability in the stratified two-fluid system, in *Proceedings of Nuclear Energy in Central Europe '99* (1999), p. 201.
13. G. Černe, S. Petelin, and I. Tiselj, Numerical errors of the volume-of-fluid interface tracking algorithms, *Int. J. Numer. Meth. Fluids*, to appear.
14. J. B. Daly, Numerical study of Two Fluid Rayleigh–Taylor instability, *Phys. Fluids* **10**, 297 (1967).

15. D. A. Drew, Mathematical modeling of two-phase flow, *Annu. Rev. Fluid Mech.* **15**, 261 (1983).
16. J. H. Ferziger and M. Perič, *Computational Methods for Fluid Dynamics* (Springer-Verlag, Heidelberg, 1996), p. 104.
17. C. L. Gardner, J. Glimm, O Mcbryan, R. Menikoff, D. H. Sharp, and Q. Zhang, The dynamics of bubble growth for Rayleigh–Taylor unstable interfaces, *Phys. Fluids* **31**, No. 3, 447 (1988).
18. J. Glimm, X. L. Li, R. Menikoff, D. H. Sharp, and Q. Zhang, A numerical study of bubble interactions in Rayleigh–Taylor instability for compressible fluids, *Phys. Fluids* **A 2**, 2046 (1990).
19. D. Gueyffier, J. Li, A. Nadim, R. Scardovelli, and S. Zaleski, Volume-of-fluid interface tracking with smoothed surface stress methods for three-dimensional flows, *J. Comput. Phys.* **152**, 423 (1999).
20. J. Han and G. Tryggvason, Secondary breakup of axisymmetric liquid drops. I. Acceleration by a constant body force, *Phys. Fluids* 3650 (1999).
21. F. H. Harlow and J. E. Welch, Numerical calculation of time-dependent viscous incompressible flow of fluid with free surface, *Phys. Fluids* **8**, 2182 (1965).
22. C. W. Hirt, A. A. Amsden, and J. L. Cook, An arbitrary Lagrangian–Eulerian computing method for all flow speeds, *J. Comput. Phys.* **14**, 227 (1974).
23. C. W. Hirt and B. D. Nichols, Volume of fluid (VOF) method for the dynamics of free boundaries, *J. Comput. Phys.* **39**, 201 (1981).
24. L. M. Hyman, Numerical methods for tracking interfaces, *Physica* **12D**, 396 (1984).
25. O. J. Ilegbusi, M. Mat, and M. J. Andrews, Effect of Atwood number on kinematic mixing of two fluids, *J. Mater. Process. Manufact. Sci.* **4**, 323 (1996).
26. M. Ishii, *Thermo-Fluid Dynamic Theory of Two-Phase Flow* (Eyrolles, Paris, 1975).
27. M. Ishii and N. Zuber, Drag coefficient and relative velocity in bubbly, droplet or particulate flows, *AIChE J.* **25**, No. 5, 843 (1979).
28. D. Jacqmin, Calculation of two-phase Navier–Stokes flows using phase field modeling, *J. Comput. Phys.* **155**, 96 (1999).
29. D. Jurić and G. Tryggvason, Computations of boiling flows, *Int. J. Multiphas. Flow* **24**, No. 3, 387 (1998).
30. F. J. Kelecy and R. H. Pletcher, The development of a free surface capturing approach for multidimensional free surface flows in closed containers, *J. Comput. Phys.* **138**, 939 (1997).
31. B. Lafaurie, C. Nardone, R. Scardovelli, S. Zaleski, and G. Zanetti, Modelling merging and fragmentation in multiphase flows with SURFER, *J. Comput. Phys.* **113**, 134 (1994).
32. M. D. Mat and O. J. Ilegbusi, Kinematic mixing of two fluids with valve perturbation, *Int. J. Multiphas. Flow* **23**, 1043 (1997).
33. A. Minato, K. Takamori, and N. Ishida, *Numerical method for Interaction Between Gas-Liquid Two-Phase Flow and Solid Motion, Two-Phase Flow Modelling and Experimentation* 1999, p. 1537 (1999).
34. C. Morel, N. Goreaud, and J. M. Delhaye, The local volumetric interfacial area transport equation: Derivation and physical significance, *Int. J. Multiphas. Flow* **25**, 1099 (1999).
35. W. Mulder, S. Osher, and J. A. Sethian, Computing interface motion in compressible gas dynamics, *J. Comput. Phys.* **100**, 209 (1992).
36. S. Osher and J. A. Sethian, Fronts propagating with curvature-dependent speed: Algorithms based on Hamilton–Jacobi formulations, *J. Comput. Phys.* **79**, 12 (1988).
37. E. G. Puckett, A. S. Almgren, J. B. Bell, D. L. Marcus, and W. J. Rider, A high order projection method for tracking fluid interfaces in variable density incompressible flows, *J. Comput. Phys.* **130**, 269 (1997).
38. W. J. Rider and D. B. Kothe, Reconstructing volume tracking, *J. Comput. Phys.* **141**, 112 (1998).
39. M. Rudman, A volume-tracking method for incompressible multifluid flows with large density variations, *Int. J. Numer. Meth. Fluids* **29**, 357 (1998).
40. J. A. Sethian, *Level Set Methods* (Cambridge Univ. Press, Cambridge, UK, 1998).
41. H. Städtke, A. Blahak, and B. Worth, Modelling of transport of interfacial area concentration in two-phase flow systems, in *NURETH-8, Proceedings* (1997), Vol. 1, p. 69.
42. H. B. Steward, Two-phase flow: Models and methods, *J. Comput. Phys.* **56**, 363 (1984).

43. M. Sussman, P. Smereka, and S. Osher, A level set approach for computing solutions to incompressible two-phase flow, *J. Comput. Phys.* **114**, 146 (1994).
44. I. Tiselj and S. Petelin, Modelling of two-phase flow with second-order accurate scheme, *J. Comput. Phys.* **136**, 503 (1997).
45. S. O. Unverdi and G. Tryggvason, A front-tracking method for viscous, incompressible, multi-fluid flows, *J. Comput. Phys.* **100**, 25 (1992).
46. S. O. Unverdi and G. Tryggvason, Computations of multi-fluid flows, *Physica* **D 60**, 70 (1992).
47. G. B. Wallis, *One-Dimensional Two-Phase Flow* (McGraw-Hill, New York, 1969).
48. O. Vbbink and R. I. lssa, A method for capturing sharp fluid interfaces on arbitrary meshes, *J. Comput. Phys.* **153**, 26 (1999).